RSC Advances

PAPER

View Article Online
View Journal | View Issue

Cite this: *RSC Adv.*, 2024, **14**, 11914

Influences of Ru and ZrO_2 interaction on the hydroesterification of styrene†

Fei Xue,‡[a] Fang Wang, ‡[a] Min Liao,[b] Mengli Liu,[a] Qunye Hong,[c] Zhen Li,*[a] Chungu Xia*[a] and Jinbang Wang *[c]

Received 3rd January 2024
Accepted 8th April 2024

DOI: 10.1039/d4ra00054d

rsc.li/rsc-advances

Interfacial Lewis acid–base pairs are commonly found in ZrO_2-supported metal catalysts due to the facile generation of oxygen vacancies of ZrO_2. These pairs have been reported to play a crucial role in olefin hydroesterification, especially in the absence of acid promoters and ligands. In this study, a series of ZrO_2-supported Ru catalysts with ruthenium(III) chloride and ruthenium(III) acetylacetonate as precursors were prepared for the styrene hydroesterification. The catalysts were thoroughly characterized by TPR, TEM, EPR, XPS, and FTIR. The Ru precursors significantly influenced the size and electronic properties of Ru clusters, albeit having minimal impact on oxygen vacancies. Mechanistic studies of styrene hydroesterification over ZrO_2-supported Ru catalysts revealed that the carbon monoxide insertion followed the hydrogen transfer step to activated styrene. Higher activity is exhibited over ZrO_2-supported Ru catalysts prepared with ruthenium(III) chloride as a precursor, attributed to the lower adsorption strength of CO over Ru clusters, as evidenced by FTIR and DFT calculations.

1. Introduction

Metal oxide-supported catalysts play a crucial role as heterogeneous catalysts, finding extensive applications in industries such as petroleum, chemicals, and environmental sectors. Among these catalysts, ZrO_2 stands out as the sole single-metal oxide possessing four distinctive chemical properties, namely acidity, basicity, reducibility, and oxidizability.[1,2] Notably, oxygen vacancies (Vö) can be easily generated in ZrO_2 due to its reducible nature. This characteristic property enhances the unique interaction between the metal and the support when ZrO_2 is utilized as a carrier, imparting significant relevance to the catalytic system.

The interaction between the metal and support stands out as the pivotal factor influencing the performance of oxide-supported catalysts, attracting more and more attention in recent years.[3–13] Given the relatively low reducibility of ZrO_2, the manifestation of strong metal–support interaction (SMSI), characterized by the partial encapsulation of the metal nanoparticles with a partially reduced oxide layer is seldom observed in the ZrO_2-supported metal catalysts under commonly employed reduction conditions. However, the introduction of oxygen vacancies in ZrO_2 can lead to the charge transfer between ZrO_2 and the supported metal, giving rise to electronic metal–support interactions (EMSIs) that significantly impact the catalyst performance. For instance, in the case of Ru/ZrO_2, the introduction of oxygen vacancies in Ru/ZrO_2 resulted in an increase in the energy of CO adsorption on the Ru site close to the oxygen vacancy. This was attributed to the charge transfer from the oxygen vacancy to Ru nanoparticles, subsequently enhancing the activity of CO_2 methanation on Ru/ZrO_2.[14] Conversely, the transfer of charge from Ru nanoparticles to ZrO_2 has also been reported by Pacchioni *et al.*[15] The EMSIs are believed to be intricately linked to factors such as metal and oxide compositions, surface structures, and sizes.[16] Therefore, different EMSIs could occur between the same metal and support.

The hydroesterification of olefins with carbon monoxide (CO) and alcohols is a highly sought-after transformation due to its atomic-economic advantage in forming both C–C and C–O bonds.[17–19] Homogeneous catalytic systems employing Pd-complexes are frequently used to facilitate this transformation, wherein acid promoters are deemed essential for the formation of Pd hydride species according to the generally accepted reaction mechanism.[20–23] However, challenges such as catalyst separation in Pd-complexes catalytic system and the high cost of palladium underscore the importance of developing a heterogeneous catalytic system with a cos-effective metal. Wang *et al.*[24,25] have reported that ceria-supported Ru-clusters catalysts exhibit high activity in catalysing olefins with CO and methanol to form corresponding esters without the need for additional acid promoters and ligands. This exceptional catalytic activity is

[a]State Key Laboratory for Oxo Synthesis and Selective Oxidation, Lanzhou Institute of Chemical Physics, Chinese Academy of Sciences, Lanzhou 730000, P. R. China. E-mail: zhenli@licp.cas.cn; cgxia@licp.cas.cn

[b]Ganzhou Branch of Jiangxi Tobacco Corporation, Ganzhou 341000, P. R. China

[c]Zhengzhou Tobacco Research Institute of CNTC, Zhengzhou 450001, P. R. China. E-mail: wangjinbangok@126.com

† Electronic supplementary information (ESI) available. See DOI: https://doi.org/10.1039/d4ra00054d

‡ These authors contributed equally to this work.

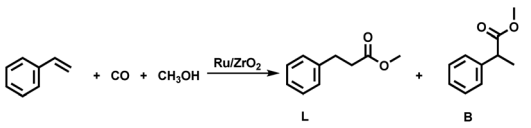

Scheme 1 The hydroesterification of styrene over Ru/ZrO_2.

attributed to the presence of interfacial Lewis acid–base pair (Ru–O–Ce–Vö) in the catalysts. ZrO_2-supported Ru catalysts have been extensively utilized in hydrogenation,[26–28] oxidation,[29] reforming,[30] and various other reactions. Considering the facile generation of the oxygen vacancies in ZrO_2 as mentioned above, ZrO_2-supported Ru catalyst hold the potential for excellent performance in the hydroesterification of olefins. Nevertheless, there is a noticeable dearth of research on such catalysts in olefin hydroesterification.

Herein, hydroesterification of styrene with CO and methanol (Scheme 1) was used as a probe reaction to systematically investigate the impact of the interaction between Ru nanoparticles and ZrO_2. A series of Ru/ZrO_2 catalysts were prepared using impregnation method, employing ruthenium(III) chloride and ruthenium(III) acetylacetonate as Ru precursors. The structure of catalysts was studied by XPS, TEM, EPR, and FTIR. The results reveal a significant influence of Ru precursor on the interaction between Ru nanoparticles and ZrO_2. Furthermore, we used infrared technology to reveal the underline mechanism of the hydroesterification of styrene over Ru/ZrO_2. Interestingly, the results indicate that the insertion of carbon monoxide followed the step of hydrogen transfer to activated styrene, resembling to the Pd-hydride mechanism.

2. Experimental

2.1 ZrO_2 synthesis and catalyst preparation

ZrO_2 supports were synthesized using a modified hydrothermal method according to the literature.[31] Typically, 3.7 g of $ZrO(NO_3)_2$, 9.6 g of urea, and 40 g of ultrapure H_2O were added to a 200 mL round-bottom flask with stirring at 70 °C. After the dissolution, the mixture was transferred to an autoclave with a polytetrafluoroethylene lining (100 mL) and maintained at 160 °C for 24 h. The resulting solid product was thoroughly washed with ultrapure water, separated through centrifugation, and dried at 80 °C overnight, followed by calcination at a specific temperature for 4 h.

The catalyst was prepared following the subsequent procedure. Initially, the ZrO_2 was impregnated with a solution of ruthenium precursor at room temperature, then dried at 100 °C for 24 h. Subsequently, the samples above underwent calcination in air at 400 °C for 3 h, followed by activation through a reduction process using $5\%H_2/Ar$ at 400 °C for 3 h, at a flow rate of 30 mL min^{-1}. The Ru loading content in all the catalysts was 1.0 wt% based on the amount of ZrO_2. The as-prepared catalysts are remarked as $1\%Ru(x)/ZrO_2(y)$, where x designates the Ru precursor (Cl: ruthenium(III) chloride, acac: ruthenium(III) acetylacetonate) and y represents the calcination temperature of ZrO_2.

2.2 Catalysts characterization

Pore and specific surface properties were acquired at −196 °C by a Micromeritics TriStar II 3020 sorption analyser. All samples were outgassed at 120 °C for 3 h under vacuum to remove moisture and volatile impurities before the measurements. A Rigaku SmartLab SE diffractometer was used to record X-ray diffraction (XRD) patterns operated at 40 kV and 40 mA using Ni-filtered Cu Kα ($\lambda = 0.15406$ nm) radiation. Transmission electron microscopy (TEM) images were observed on an FEI Tecnai G′ F20 S-Twin electron microscope operated at 200 kV. Fourier transform infrared (FTIR) spectra were recorded using a Nicolet 6700 spectrometer. The spectrum was recorded with a spectral resolution of 4 cm^{-1} and scan times of 32. The sample was pressed into a self-supported wafer (*ca.* 20 mg cm^{-2}). Before each experiment, the sample was reduced *in situ* in the IR cell under $5\%H_2/Ar$ gas flow at 400 °C for 3 h. Subsequently, the sample was swept with Ar (99.999% purity) at 400 °C for 0.5 h. For the adsorption of CO, the sample was cooled down to 50 °C under an Ar flow rate of 30 mL min^{-1}. After cooling to 50 °C, a background spectrum was recorded. Then the sample was purged with CO for 0.5 h, followed by flushing with Ar. In order to track the intermediate species formed on the catalyst from methanol or styrene with CO, the reduced sample was cooled down to 160 °C with an Ar flow rate of 30 mL min^{-1}. Then a background spectrum was recorded under this temperature. For tracking the intermediate species formed on the catalyst from methanol with CO, methanol was first introduced into the cell from the methanol bubbler using Ar gas with a flow rate of 30 mL min^{-1}, and then the Ar gas was switched to CO. For tracking the intermediate species formed on the catalyst from styrene with CO, styrene was first introduced into the cell from the styrene bubbler with an Ar flow rate of 30 mL min^{-1}, and then the Ar gas was switched to CO. For tracking the intermediate species formed on the catalyst from methanol, styrene, and CO, methanol and styrene were simultaneously introduced into the cell with an Ar flow rate of 30 mL min^{-1} from the bubbler containing these two substances, and then the Ar gas was switched to CO. Pyridine FTIR was recorded at 50 °C. H_2 temperature-programmed reduction (TPR) was carried out on Micromeritics AutoChem II 2920. Approximately 150 mg of catalyst sample was first under pretreatment at 120 °C for 3 h in Ar (99.999% purity) with a flow rate of 30 mL min^{-1}. After cooling down to 50 °C, the gas was switched to $5\%H_2/Ar$ with a flow rate of 30 mL min^{-1}, and the reduction was carried out at a heating rate of 10 °C min^{-1}. Electron paramagnetic resonance (EPR) measurements were performed at room temperature using Bruker's WIN-EPR. X-ray photoelectron spectroscopy (XPS) was conducted on a Thermo Scientific Nexsa system, and the binding energies (BE) were calibrated with respect to the C (1s) peak of ubiquitous carbon at a binding energy of 284.8 eV.

2.3 Catalytic activity tests

The hydroesterification of styrene was carried out in a 30 mL stainless steel autoclave equipped with a magnetic stirrer. In a representative test for the hydroesterification of styrene, 2 mmol of styrene, a specified amount of catalyst, 5 mL of methanol, and 0.1 g of *n*-decane used as an internal standard

were loaded into the reactor. The autoclave was purged with CO three times to eliminate residual air inside and then charged with CO up to 0.5 MPa at room temperature. The reaction mixture was then heated to 160 °C under magnetic stirring for a duration of 6 h. After the completion of the reaction, the reactor was immediately transferred to a water bath to quench the reaction. Separation of the liquid from the solids was achieved through centrifugation, and the liquid phase was subsequently analysed using an Agilent 7890 gas chromatograph equipped with an HP-5 capillary column and an FID detector. The styrene conversion and product selectivity were calculated according to the following equations:

$$\text{Conversion } [\%] = \sum n_i / n_{\text{styrene}} \times 100,$$

$$\text{Selectivity } [\%] = n_i / \sum n_i \times 100,$$

where n_i represents the molar quantity of product i and n_{styrene} is the molar quantity of styrene introduced into the reaction system.

2.4 Computational details

The periodic DFT slab calculations for the adsorption of CO on Ru_3/m-$ZrO_2(-111)_{Vö}$ and Ru_7/m-$ZrO_2(-111)_{Vö}$ were carried out employing the ultrasoft pseudopotentials[32] and the spin polarized generalized gradient approximation (GGA) exchange-correlation functional proposed by Perdew, Burke, and Ernzerhof (PBE),[33] as implemented in CASTEP suite of programs.[34] Grimme method was used for dispersion corrections.[35] To optimize Ru_3, Ru_7, m-$ZrO_2(-111)$ surface, and CO adsorption on m-$ZrO_2(-111)$ surface, spin polarized functional was used. An energy cutoff of 340 eV was applied for the plane-wave expansion of the electronic eigenfunctions of m-$ZrO_2(-111)$ surface. The surface Brillouin zone was sampled with a gamma point. The m-$ZrO_2(-111)$ surface was modelled with a periodic three-layer slab with the 2×2 ($Zr_{48}O_{96}$) unit cell. In current work, one O–Zr–O trilayer of ZrO_2 is defined as a monolayer. The periodically repeated slabs were separated with a vacuum thickness of 15 Å in order to avoid the neighbouring slab interactions along *z*-axis. The convergence criteria for geometry optimization were set to 0.05 (for the local minima) for maximum force, 1.0×10^{-5} eV per atom for energy, 1.0×10^{-6} eV per atom for SCF, and 0.001 Å for maximum displacement. The lattice constant for bulk ZrO_2 was predicted to be $a = 5.131$ Å, $b = 5.234$ Å, $c = 5.351$ Å and $\beta = 99.1$, which is in good agreement with the experimental values of $a = 5.169$ Å, $b = 5.232$ Å and $c = 5.341$ Å, $\beta = 99.2$.[36] The adsorption energy of CO on Ru_3/m-$ZrO_2(-111)_{Vö}$ and Ru_7/m-$ZrO_2(-111)_{Vö}$ is defined as: $\Delta E = E(\text{CO/slab}) - [E(\text{CO}) + E(\text{slab})]$, where E(CO/slab) is the total energy for the slab with the adsorbed CO molecule on the surface, E(CO) is the total energy of the free CO molecule, and E(slab) is the total energy of the bare slab of the Ru_3/m-$ZrO_2(-111)_{Vö}$ or Ru_7/m-$ZrO_2(-111)_{Vö}$.

3. Results and discussion

The thermal stability of dried ZrO_2 was assessed through TG to determine an appropriate calcination temperature for catalyst preparation. The TG curve illustrated in Fig. 1a, reveals weight loss before 120 °C, attributed to the water volatilization, and a considerable weight loss between 120 °C and 500 °C, possibly due to the condensation of hydroxyl groups. Notably, no apparent weight loss is observed above ~500 °C. Experimentally, no apparent weight loss was detected when the calcination temperature of ZrO_2 was higher than 400 °C, which may be due to the slow heating rate (3 °C min^{-1}) and long holding time (4 h) used in this study. Therefore, the calcination temperature ranging from 400 °C to 600 °C was chosen to obtain ZrO_2 with stable mass, thereby ensuring the consistent loading of Ru added to the reaction system.

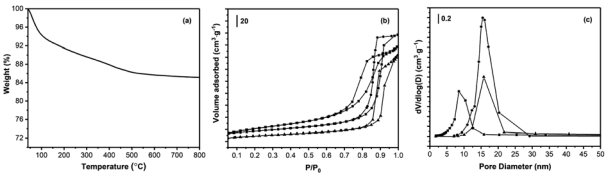

Fig. 1 (a) TG curve of dried ZrO_2; (b) N_2 adsorption–desorption isotherms of calcined ZrO_2; and (c) BJH pore size distribution of calcined ZrO_2. (■) ZrO_2(400), (●) ZrO_2(500), (▲) ZrO_2(600).

As shown in N_2 adsorption–desorption isotherms of calcinated ZrO_2 (Fig. 1b), all samples exhibit type IV isotherms with a H1 hysteresis loop, indicating that the calcined ZrO_2 is a porous material composed of agglomerates or compacts of approximately uniform spheres in fairly regular array.[37] Therefore, the calcined ZrO_2 possesses a narrow distributions of pore size (Fig. 1c). The detailed physical structure properties of ZrO_2 calcinated from 400 °C to 600 °C were listed in Table S1.† The calcination temperature exerted a more pronounced impact on the specific surface area (S_{BET}) and pore size of the support compared to the pore volume. The pore volume of ZrO_2 remains relatively at ~0.24 $cm^3\ g^{-1}$ and changes little across the studied calcination temperatures. However, the S_{BET} of ZrO_2 decreases from 81 $m^2\ g^{-1}$ to 34 $m^2\ g^{-1}$ with an increase in calcination temperature from 400 °C to 600 °C. Concurrently, the pore size of ZrO_2 undergoes an increase from 8.5 nm to 15.8 nm during the same temperature variation.

The results of the hydroesterification of styrene on the catalysts are listed in Table 1. The hydroesterification of styrene on ZrO_2 as a blank experiment was also conducted, and no product was detected. With an increase in the calcination temperature of ZrO_2 from 400 °C to 600 °C, the styrene conversion decreased from 57.4% to 21.9% for the 1%Ru(Cl)/ZrO_2. However, the selectivity towards ester (L + B) increased from 79.8% to 94.0% with the calcination temperature of ZrO_2. The ester yield reached its maximum of 45.8% over the 1% Ru(Cl)/ZrO_2(400) catalyst in this study. Conversely, when the Ru precursor was changed to ruthenium(III) acetylacetonate, the conversion and selectivity were considerably lower at only 4.6% and 70.3%, respectively. The amount of residual Cl detected by XPS is negligible. Therefore, the substantial difference in the catalytic performance between 1%Ru(Cl)/ZrO_2(400) and 1% Ru(acac)/ZrO_2(400) is likely attributed to the catalyst structure, leading to different interaction between Ru and ZrO_2.

Table 1 The hydroesterification of styrene on various catalysts[a]

Entry	Catalysts	Conversion (%)	Selectivity (%)		
			L	B	Others[b]
1	ZrO_2(400)	—	—	—	—
2	$RuCl_3 \cdot 3H_2O$	46.5	21.1	5.0	73.9
3	1%Ru(acac)/ZrO_2(400)	4.6	61.5	8.8	29.7
4	1%Ru(Cl)/ZrO_2(400)	57.4	74.3	5.5	20.2
5	1%Ru(Cl)/ZrO_2(500)	31.9	81.4	7.9	10.7
6	1%Ru(Cl)/ZrO_2(600)	21.9	83.3	10.7	6.0
7	1%Ru/SiO_2	3.0	54.5	—	45.5
8	1%Ru/Al_2O_3	2.3	52.5	—	47.5
9	1%Ru/carbon	15.7	2.0	0.9	97.1
10	1%Ru/CeO_2	2.0	15.3	6.9	77.8

[a] Reaction conditions: 2 mmol styrene, styrene/Ru = 83, 0.1 g *n*-decane, 5 mL methanol, P = 0.5 MPa, T = 160 °C, t = 6 h. [b] Other products include (1-methoxyethyl)benzene, ethylbenzene and polystyrene.

$RuCl_3 \cdot 3H_2O$ was also found to be active in the hydroesterification of styrene. Nevertheless, its selectivity towards ester products was very low. The time-dependent performance profile (Fig. 2) of 1%Ru(Cl)/ZrO_2(400) indicates that the conversion of styrene increased to >99% after 16.2 h reaction with the selectivity towards L and B changed little with time after 3 h reaction. Removal of the Ru/ZrO_2 catalyst from the reaction system after 1.5 h reaction nearly halted the conversion, and the ester yield levelled off at ~12%, indicating heterogeneous catalysis (Fig. S5†).

The TPR measurements were conducted on the calcined samples to evaluate the redox behaviour of the studied catalysts, and the results were shown in Fig. 3a. Two peaks are observed

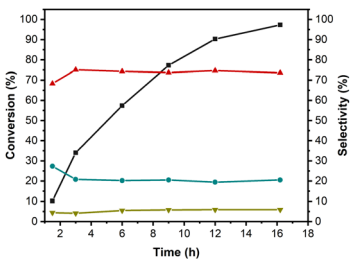

Fig. 2 Time-dependent performance profile of 1%Ru(Cl)/ZrO_2(400) catalyst. Reaction conditions: 2 mmol styrene, styrene/Ru = 83, 0.1 g *n*-decane, 5 mL methanol, P = 0.5 MPa, T = 160 °C. (■) Conversion of styrene, (▲) selectivity of L, (▼) selectivity of B, (●) selectivity of others.

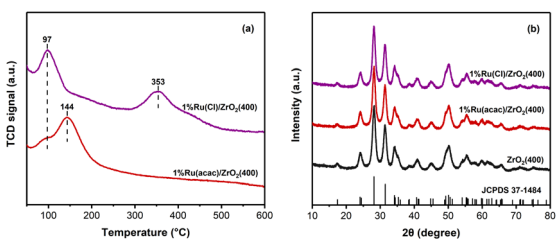

Fig. 3 (a) TPR of calcined samples and (b) XRD of reduced samples.

for 1%Ru(acac)/ZrO_2(400) and 1%Ru(Cl)/ZrO_2(400). The low-temperature peak is attributed to Ru surface oxide with little interaction with support, while the high-temperature peak is attributed to the reduction of Ru species with strong interaction with support.[30] Interestingly, although the first reduction peak of both catalysts is nearly at the same position (97 °C), the second reduction peak of 1%Ru(Cl)/ZrO_2(400) is significantly higher than that of 1%Ru(acac)/ZrO_2(400) (353 °C *vs.* 144 °C), indicating a much stronger interaction between Ru clusters and nano ZrO_2 for 1%Ru(Cl)/ZrO_2(400). Moreover, assuming complete reduction of Ru species in 1%Ru(acac)/ZrO_2(400), ~2% of Ru species in 1%Ru(Cl)/ZrO_2(400) remains unreduced. The XRD analysis of reduced samples revealed that nano ZrO_2 remains a monoclinic phase, consistent with the TEM (Fig. S1†). The loading of ruthenium has negligible effects on its crystalline structure and bulk structure (Fig. 3b), and the average crystallite size of nano ZrO_2 in the reduced sample is ~12.1 nm, as determined using the Scherrer equation with 2θ at ~28.2° ((−111) plane). Furthermore, the XRD did not reveal the presence of Ru phases, implying the tiny size of Ru nanoparticles in the catalysts fitting to the TEM results.

The EPR spectra of reduced samples were illustrated in Fig. 4a. Two signals at g = 1.974 and g = 1.956 are observed for nano ZrO_2(400), indicating the presence of Zr^{3+}.[38] The signal at g = 2.090 in 1%Ru(acac)/ZrO_2(400) is usually assigned to Ru^{3+}.[39,40] However, no Ru^{3+} species were detected in the XPS and CO-FTIR analysis (as shown in Fig. 4b and c). This discrepancy could be attributed to the low concentration of Ru^{3+} in the 1%Ru(acac)/ZrO_2(400) or the possibility that the Ru^{3+} species have been incorporated into the nano ZrO_2 framework, making them difficult to detect using surface techniques. On the other hand, the Ru^{3+} signal in 1%Ru(Cl)/ZrO_2(400) is significantly weaker compared to the signal in 1%Ru(acac)/ZrO_2(400). This discrepancy appears to contradict the results obtained from the TPR analysis. In fact, antiferromagnetic coupling also results in a decrease in the intensity of EPR.[41] Therefore, stronger antiferromagnetic coupling occurred in 1%Ru(Cl)/ZrO_2(400). The signal at g = 2.004 is ascribed to Vö. Generally, the introduction of metals, especially at the metal-oxide interface, is conducive to the formation of oxygen vacancies in oxide supports.[42,43] However, in this study, little variation was observed in the intensity of the Vö signal and a decrease in the intensity of the Zr^{3+} signal upon the addition of Ru. This phenomenon is peculiar as it deviates the commonly accepted relationship between the formation of oxygen vacancies and the concentration of Zr^{3+}. Typically, the formation of oxygen vacancies is represented by the equation $O^{2-} \leftrightarrow 1/2O_2 + Vö + 2e^-$, followed by $Zr^{4+} + e^- \leftrightarrow Zr^{3+}$. According to this representation, the number of oxygen vacancies should be directly proportional to the concentration of Zr^{3+}. However, the observed trend in this study contradicts this expected linear correlation. There are two possible explanations for the decrease in Zr^{3+} signal. One possibility is the transfer of electron from Zr^{3+} to Ru clusters. Another possible explanation is that Zr^{3+} and Ru clusters are antiferromagnetically coupled *via* O^{2-}. XPS results indicated that the percentage of Zr^{3+} changed little in the catalysts (Table S2†). Although the electron transfer between Zr^{3+} and Ru

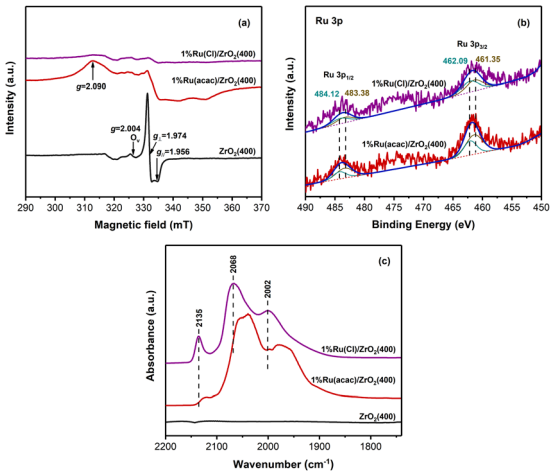

Fig. 4 (a) EPR spectra of reduced samples; (b) XPS of Ru 3p of the reduced sample; and (c) *in situ* FTIR of CO adsorption on the reduced sample.

clusters cannot be completely ruled out, it is likely to be minimal. Therefore, the reduction in the Zr^{3+} signal is likely primarily attributed to antiferromagnetic coupling between Zr^{3+} and Ru species. Moreover, the Zr^{3+} signal in 1%Ru(Cl)/ZrO_2(400) decreased more than that in 1%Ru(acac)/ZrO_2(400), showing stronger antiferromagnetic coupling in 1%Ru(Cl)/ZrO_2(400). This enhanced coupling may be a result of the stronger interaction between metal and support and/or larger Ru clusters in 1%Ru(Cl)/ZrO_2(400).

The charge state of the Ru species was analysed using the Ru 3p signal, as the Ru 3d signal overlaps with the C 1s signal. The 3p peak of Ru was split into two peaks using Avantage software. Peaks observed at approximately 461.35 eV and 483.38 eV are attributed to Ru^0 $3p_{3/2}$ and $3p_{1/2}$, respectively. Additionally, peaks at approximately 462.09 eV and 484.12 eV are assigned to $Ru^{\delta+}$ $3p_{3/2}$ and $3p_{1/2}$, respectively. The signal intensity of Ru in the 1%Ru(Cl)/ZrO_2(400) is found to be lower than that of the 1% Ru(acac)/ZrO_2(400), indicating a larger Ru clusters in 1%Ru(Cl)/ZrO_2(400). Furthermore, the ratio of $Ru^{\delta+}/Ru^0$ in the 1%Ru(Cl)/ZrO_2(400) is higher than that in the 1%Ru(acac)/ZrO_2(400), suggesting that the reduction of Ru species is more difficult in 1%Ru(Cl)/ZrO_2(400), consistent with the results of TPR.

As illustrated in Fig. 4c, no notable peaks corresponding to CO adsorption are observed on ZrO_2(400). However, three distinct peaks appear at 2120–2140 cm^{-1}, 2030–2070 cm^{-1}, and 1980–2010 cm^{-1} for 1%Ru(acac)/ZrO_2(400) and 1%Ru(Cl)/ZrO_2(400). According to previous studies,[24,44] the two high-frequency bands in the spectrum are believed to be associated with CO adsorption on $Ru^{\delta+}$ sites. However, there is no consensus on the oxidation state of $Ru^{\delta+}$. The low-frequency band is generally agreed to result from linear CO adsorption on metal crystallites.[24,44] The lower CO adsorption intensity on 1%Ru(Cl)/ZrO_2(400) compared to 1%Ru(acac)/ZrO_2(400) may be attributed to the presence of larger Ru clusters on 1%Ru(Cl)/ZrO_2(400), as supported by the XPS results. It is noteworthy that all the peaks associated with CO adsorption on 1%Ru(acac)/ZrO_2(400) are shifted towards lower wavenumbers (red-shifted) compared to those on 1%Ru(Cl)/ZrO_2(400). The CO adsorption mechanism on metals is typically explained by a donation–backdonation process, in which, electrons from the occupied σ(CO) orbital donate to the metal (σ(CO)–d(Ru)) and back-donate from the metal to the unoccupied π* state of CO (d(Ru)–π*(CO)). An increase in the charge density of the metal results in more charge being transferred to the unoccupied π* state of CO, leading to a red shift in the CO adsorption peaks in FTIR spectra. Therefore, the observed red shift of the CO adsorption peaks on 1%Ru(acac)/ZrO_2(400) compared to 1% Ru(Cl)/ZrO_2(400) suggests a higher charge density in the Ru clusters of 1%Ru(acac)/ZrO_2(400), in agreement with the findings from XPS studies. Furthermore, the weaker antiferromagnetic coupling between Ru and Zr^{3+} may also contribute to the significant redshift observed in CO adsorption on 1%Ru(acac)/ZrO_2(400), as the Ru clusters in 1%Ru(acac)/ZrO_2(400) with more uncoupled electrons may back-donate more charge to CO.

The mechanism of styrene hydroesterification was investigated by *in situ* FTIR (Fig. 5). In the olefin hydroesterification catalysed by Pd-complexes, two predominant mechanisms exist, as shown in Scheme 2: the Pd-acyl mechanism and the Pd-hydride mechanism.[22,45] A key distinction between both mechanisms lies in the reaction order of CO and olefins. In the Pd-acyl mechanism, CO reacts prior to olefins, whereas in the Pd-hydride mechanism, olefins react first with the palladium

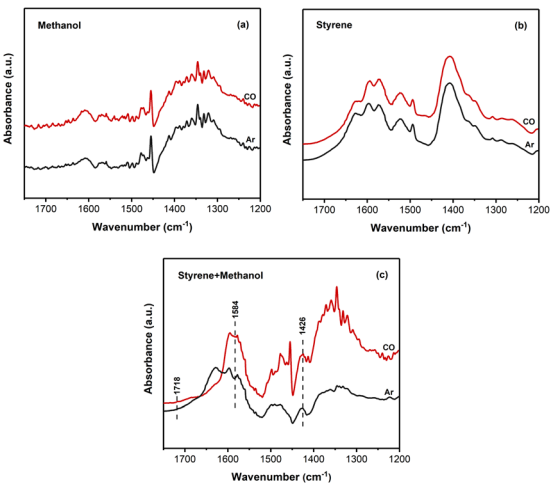

Fig. 5 *In situ* FTIR spectra of (a) methanol adsorption, (b) styrene adsorption, and (c) the hydroesterification of styrene over 1%Ru(Cl)/ZrO_2(400) at 160 °C under Ar and CO.

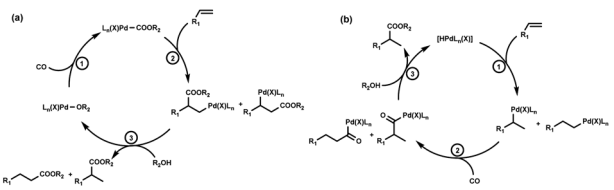

Scheme 2 Proposed mechanisms for the olefin hydroesterification catalysed by Pd-complexes: (a) Pd-acyl mechanism and (b) Pd-hydride mechanism.

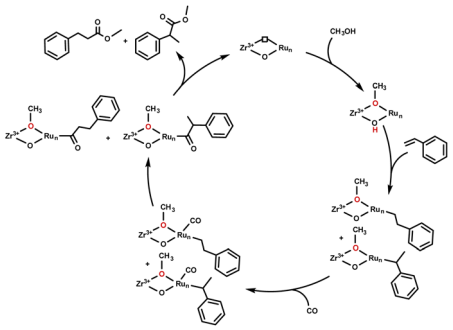

Scheme 3 Proposed mechanisms for styrene hydroesterification on Ru/ZrO_2.

complex before CO is added. The hypothesis tested was whether the catalytic mechanism of Ru/ZrO_2 is similar to the Pd-acyl mechanism. If so, the presence of a C=O absorption peak should be observed in the FTIR spectra when both CO and methanol are added to the reaction system simultaneously. To test this, methanol was first introduced into a 1%Ru(Cl)/ZrO_2(400) system using Ar as the carrier gas, and then switched to CO while monitoring the process using FTIR. The resulting FTIR spectra are displayed in Fig. 5a. Minimal variation in the FTIR spectra after changing Ar to CO indicated that the catalytic mechanism of Ru/ZrO_2 for olefin hydroesterification is not analogous to that of Pd-acyl. Therefore, it is supposed that the catalytic mechanism of Ru/ZrO_2 for olefin hydroesterification may resemble that of Pd-hydride. Further experiments involved introduced styrene into the 1%Ru(Cl)/ZrO_2(400) by Ar and CO, respectively, and monitored the process using FTIR. The results reveal that no peak ascribed to C=O appears in the FTIR after the introduction of styrene into the 1%Ru(Cl)/ZrO_2(400) by CO (Fig. 5b). It is not unexpected, suggesting that the hydrogen species in 1%Ru(Cl)/ZrO_2(400) may not be the active species for the olefin hydroesterification. Importantly, the amount of Brønsted acid sites is negligible in the 1%Ru(Cl)/ZrO_2(400) (Fig. S4†). As demonstrated in Fig. 5c, three adsorption peaks were observed at 1718 cm^{-1}, 1584 cm^{-1}, and 1426 cm^{-1} when methanol and styrene were simultaneously introduced into 1% Ru(Cl)/ZrO_2(400) by CO. These peaks are attributed to ν(C=O), νas(OCO), and νs(OCO), respectively. This indicates that the hydrogen species derived from methanol may be the active species for olefin hydroesterification. Therefore, the hydroesterification of styrene over Ru/ZrO_2 may follow a mechanism similar to that proposed by Wang *et al.*[24] for the hydroesterification of ethylene over Ru/CeO_2. In this mechanism, methanol dissociation and the transfer of hydrogen to activated ethylene occur on Ru–O–Ce–Vö. Based on these findings, a potential mechanism was proposed for the hydroesterification of styrene on Ru/ZrO_2, as outlined in Scheme 3.

As indicated by the mechanism discussed above, the activation of CO begins on Ru clusters, followed by the insertion of CO between the metal and the alkyl group. Consequently, the strength of CO adsorption on Ru clusters may play a crucial role in CO insertion, ultimately impacting the efficiency of the catalyst. Besides, the strength of CO adsorption over Ru/ZrO_2 is

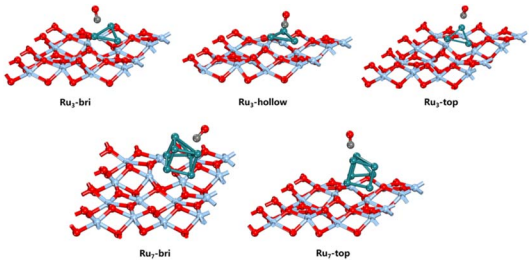

Fig. 6 The optimized geometries of CO adsorption on Ru_3/m-$ZrO_2(-111)_{Vö}$ and Ru_7/m-$ZrO_2(-111)_{Vö}$.

Table 2 CO adsorption energies, Ru–C and C–O distance for CO adsorption on Ru_3/m-$ZrO_2(-111)_{Vö}$ and Ru_7/m-$ZrO_2(-111)_{Vö}$

		Bond distance (Å)	
Adsorption sites	Δ*E* (eV)	d_{Ru-C}	d_{C-O}
Ru_3-bri	−2.35	1.811	1.186
Ru_3-hollow	−2.92	1.961	1.217
Ru_3-top	−2.66	2.057	1.234
Ru_7-bri	−1.94	1.887	1.187
Ru_7-top	−2.15	2.119	1.217

also calculated by DFT. Based on the above results, monoclinic polymorph ZrO_2 (m-ZrO_2) with the most stable (−111) surface and Vö is selected as a model. Ru_3 clusters and Ru_7 clusters (3 Ru atoms for the top layer and 4 Ru atoms for the sublayer) are chosen to represent Ru/ZrO_2 catalysts prepared with ruthenium(III) acetylacetonate and ruthenium(III) chloride as precursors respectively. The optimized geometries of CO adsorption on Ru_3/m-$ZrO_2(-111)_{Vö}$ and Ru_7/m-$ZrO_2(-111)_{Vö}$ are shown in Fig. 6, and CO adsorption energies (in eV), Ru–C and C–O distance (in Å) are listed in Table 2. The CO adsorption energies at the top and bridge sites of Ru_7 are lower than those of the corresponding sites of Ru_3, decreasing by 0.51 eV and 0.41 eV, respectively. Therefore, the higher activity of 1%Ru(Cl)/ZrO_2(400) in the styrene hydroesterification is attributed to its lower adsorption strength of CO on Ru clusters, which is favourable for the insertion of CO to Ru–C bond.

4. Conclusions

In summary, the hydroesterification of styrene with methanol and CO was effectively catalysed on Ru/ZrO_2, yielding 57.4% styrene conversion and 79.8% ester (L + B) selectivity over 1% Ru(Cl)/ZrO_2(400) at 0.5 MPa CO and 160 °C for 6 h. Mechanistic studies on the hydroesterification of styrene with methanol and carbon monoxide over Ru/ZrO_2 catalysts, as determined by FTIR, revealed that the insertion of carbon monoxide followed the step of hydrogen transfer to activated styrene. The interaction between Ru and ZrO_2 can be significantly influenced by the Ru precursor. Larger Ru cluster size, higher $Ru^{\delta+}$ concentrations and stronger antiferromagnetic coupling were observed with ruthenium(III) chloride as the precursor. The lower adsorption strength of CO over Ru clusters for 1%Ru(Cl)/ZrO_2(400) may

improve CO insertion in the Ru–C bond, thus increasing the styrene conversion.

Conflicts of interest

There are no conflicts to declare.

Notes and references

1 P. D. L. Mercera, J. G. V. Ommen, E. B. M. Doesburg, A. J. Burggraaf and J. R. H. Ross, *J. Mater. Sci.*, 1992, **27**, 4890–4898.
2 K. Tanabe, *Mater. Chem. Phys.*, 1985, **13**, 347–364.
3 H. Frey, A. Beck, X. Huang, J. A. v. Bokhoven and M. G. Willinger, *Science*, 2022, **376**, 982–987.
4 Y. Li, Y. Zhang, K. Qian and W. Huang, *ACS Catal.*, 2022, **12**, 1268–1287.
5 K. W. Jeon, H. J. Byeon, H. M. Kim, B. Choe, C. H. Jeong, T. Y. Choi, W. Won and D. W. Jeong, *ACS Sustain. Chem. Eng.*, 2022, **10**, 6289–6303.
6 Q. Li, X. Chu, Y. Wang, Q. Yang, Z. Su, Y. Peng, W. Si and J. Li, *ACS Catal.*, 2022, **12**, 4430–4439.
7 M. J. Zachman, V. Fung, F. Polo-Garzon, S. Cao, J. Moon, Z. Huang, D. E. Jiang, Z. Wu and M. Chi, *Nat. Commun.*, 2022, **13**, 3253.
8 C. Zheng, D. Mao, Z. Xu and S. Zheng, *J. Catal.*, 2022, **411**, 122–134.
9 X. C. Sun, K. Yuan, J. H. Zhou, C. Y. Yuan, H. C. Liu and Y. W. Zhang, *ACS Catal.*, 2021, **12**, 923–934.
10 S. Sun, X. Wu, Z. Huang, H. Shen, H. Zhao and G. Jing, *Chem. Eng. J.*, 2022, **435**, 135035.
11 J. Feng, L. Liu, X. Zhang, J. Wang, X. Ju, R. Li, J. Guo, T. He and P. Chen, *Catal. Sci. Technol.*, 2023, **13**, 844–853.
12 C. J. Breckner, K. Zhu, M. Wang, G. Zhang, C. W. Li and J. T. Miller, *Catal. Sci. Technol.*, 2023, **13**, 157–169.
13 S. Kaiser, J. Plansky, M. Krinninger, A. Shavorskiy, S. Zhu, U. Heiz, F. Esch and B. A. J. Lechner, *ACS Catal.*, 2023, **13**, 6203–6213.
14 S. Chen, A. M. Abdel-Mageed, M. Li, S. Cisneros, J. Bansmann, J. Rabeah, A. Brückner, A. Groß and R. J. Behm, *J. Catal.*, 2021, **400**, 407–420.
15 H. Y. T. Chen, S. Tosoni and G. Pacchioni, *J. Phys. Chem. C*, 2014, **119**, 10856–10868.
16 K. Qian, H. Duan, Y. Li and W. Huang, *Chem.–Eur. J.*, 2020, **26**, 13538–13542.
17 H. Li, K. Dong, H. Jiao, H. Neumann, R. Jackstell and M. Beller, *Nat. Chem.*, 2016, **8**, 1159–1166.
18 K. Dong, X. Fang, S. Gulak, R. Franke, A. Spannenberg, H. Neumann, R. Jackstell and M. Beller, *Nat. Commun.*, 2017, **8**, 14117.
19 C. P. Folster, R. P. Harkins, S. Y. Lo, J. D. Sachs and I. A. Tonks, *Trends Chem.*, 2021, **3**, 469–484.
20 J. Yang, J. Liu, H. Neumann, R. Franke, R. Jackstell and M. Beller, *Science*, 2019, **366**, 1514–1517.
21 K. Dong, R. Sang, X. Fang, R. Franke, A. Spannenberg, H. Neumann, R. Jackstell and M. Beller, *Angew. Chem., Int. Ed.*, 2017, **56**, 5267–5271.
22 Z. He, Z. Hou, Y. Luo, Y. Dilixiati and W. Eli, *Catal. Sci. Technol.*, 2014, **4**, 1092–1103.
23 D. B. G. Williams, M. L. Shaw, M. J. Green and C. W. Holzapfel, *Angew. Chem., Int. Ed.*, 2008, **47**, 560–563.
24 J. An, Y. Wang, J. Lu, J. Zhang, Z. Zhang, S. Xu, X. Liu, T. Zhang, M. Gocyla, M. Heggen, R. E. Dunin-Borkowski, P. Fornasiero and F. Wang, *J. Am. Chem. Soc.*, 2018, **140**, 4172–4181.
25 J. An, Y. Wang, Z. Zhang, J. Zhang, M. Gocyla, R. E. Dunin-Borkowski and F. Wang, *Chin. J. Catal.*, 2020, **41**, 963–969.
26 D. Rao, X. Xue, G. Cui, S. He, M. Xu, W. Bing, S. Shi and M. Wei, *Catal. Sci. Technol.*, 2018, **8**, 236–243.
27 R. J. Huang, Q. Q. Cui, Q. Q. Yuan, H. H. Wu, Y. J. Guan and P. Wu, *ACS Sustain. Chem. Eng.*, 2018, **6**, 6957–6964.
28 J. Ftouni, A. Muñoz-Murillo, A. Goryachev, J. P. Hofmann, E. J. M. Hensen, L. Lu, C. J. Kiely, P. C. A. Bruijnincx and B. M. Weckhuysen, *ACS Catal.*, 2016, **6**, 5462–5472.
29 C. M. Pichler, M. G. Al-Shaal, D. Gu, H. Joshi, W. Ciptonugroho and F. Schuth, *ChemSusChem*, 2018, **11**, 2083–2090.
30 H. S. Whang, M. S. Choi, J. Lim, C. Kim, I. Heo, T. S. Chang and H. S. Lee, *Catal. Today*, 2017, **293–294**, 122–128.
31 W. Li, H. Huang, H. Li, W. Zhang and H. Liu, *Langmuir*, 2008, **24**, 8358–8366.
32 D. Vanderbilt, *Phys. Rev. B: Condens. Matter Mater. Phys.*, 1990, **41**, 7892–7895.
33 J. P. Perdew, K. Burke and M. Ernzerhof, *Phys. Rev. Lett.*, 1996, **77**, 3865–3868.
34 V. Milman, B. Winkler, J. A. White, C. J. Pickard, M. C. Payne, E. V. Akhmatskaya and R. H. Nobes, *Int. J. Quantum Chem.*, 2000, **77**, 895–910.
35 S. Grimme, *J. Comput. Chem.*, 2006, **27**, 1787–1799.
36 A. Taoudi, J. P. Laval and B. Frit, *Mater. Res. Bull.*, 1994, **29**, 1137–1147.
37 K. S. W. Sing, D. H. Everett, R. A. W. Haul, L. Moscou, R. A. Pierotti, J. Rouquérol and T. Siemieniewska, *Pure Appl. Chem.*, 1985, **57**, 603–619.
38 M. Labaki, H. Laversin, E. A. Zhilinskaya, A. Aboukaïs and D. Courcot, *Catal. Commun.*, 2012, **17**, 64–70.
39 P. J. Carl and S. C. Larsen, *J. Catal.*, 2000, **196**, 352–361.
40 P. Castillo-Villalón and J. Ramírez, *J. Catal.*, 2009, **268**, 39–48.
41 J. T. Brewster, G. Anguera, M. D. Moore, B. S. Dolinar, H. Zafar, G. D. Thiabaud, V. M. Lynch, S. M. Humphrey and J. L. Sessler, *Inorg. Chem.*, 2017, **56**, 12665–12669.
42 K. Yu, L. L. Lou, S. Liu and W. Zhou, *Adv. Sci.*, 2019, **7**, 1901970.
43 A. Ruiz Puigdollers, P. Schlexer, S. Tosoni and G. Pacchioni, *ACS Catal.*, 2017, **7**, 6493–6513.
44 M. Kantcheva and S. Sayan, *Catal. Lett.*, 1999, **60**, 27–38.
45 A. Brennführer, H. Neumann and M. Beller, *ChemCatChem*, 2009, **1**, 28–41.